



# Highly efficient FeS<sub>2</sub>@FeOOH core-shell water oxidation electrocatalyst formed by surface reconstruction of FeS<sub>2</sub> microspheres supported on Ni foam



Caizhen Yue <sup>a</sup>, Xuena Zhang <sup>a</sup>, Jie Yin <sup>a,\*</sup>, Huawei Zhou <sup>a,\*</sup>, Kuo Liu <sup>b,\*</sup>, Xin Liu <sup>c</sup>

<sup>a</sup> School of Materials Science and Engineering, Liaocheng University, Liaocheng 252000, China

<sup>b</sup> Beijing Key Laboratory of Ionic Liquids Clean Process, Institute of Process Engineering, Chinese Academy of Sciences, Beijing 100190, China

<sup>c</sup> School of Resources and Materials, Northeastern University at Qinhuangdao, Qinhuangdao 066004, China

## ARTICLE INFO

### Keywords:

Water oxidation electrocatalyst  
FeS<sub>2</sub> microsphere  
Surface reconstruction  
Core-shell FeS<sub>2</sub>@FeOOH

## ABSTRACT

FeS<sub>2</sub> without dopants often exhibits poor oxygen evolution reaction (OER) performance, and development of FeS<sub>2</sub> with excellent performance for OER is still a challenge. In this study, uniform FeS<sub>2</sub> microspheres were synthesized and supported on Ni foam (NF), showing excellent OER activity with a low overpotential of 170 mV at 10 mA/cm<sup>2</sup> in 1.0 M KOH electrolyte, superior to NF, other FeS<sub>2</sub> on NF and most of Fe-containing non-noble metal OER catalysts in the existing literature (ranked top 4) under the same test conditions. The revealing of catalyst reconstruction during OER is essential for understanding the real active sites, but studies on FeS<sub>2</sub> reconstruction are rare. Herein, reconstruction of FeS<sub>2</sub> microsphere to core-shell FeS<sub>2</sub>@FeOOH during OER was observed using TEM, SEM, XRD, XPS and Raman spectroscopy. The special core-shell FeS<sub>2</sub>@FeOOH structure benefited the OER performance. This research has significance for the understanding and rational design of FeS<sub>2</sub> catalyst for OER.

## 1. Introduction

Global warming and environmental pollution caused by burning traditional fossil fuels are two major problems. Therefore, the development of clean and renewable energy has become an important research topic for scientists and engineers. Hydrogen (H<sub>2</sub>) has a high specific energy density and is considered to be an attractive alternative to fossil fuels [1,2]. One of the most effective ways to produce H<sub>2</sub> with low cost and high purity is to decompose water into H<sub>2</sub> and O<sub>2</sub> through green electricity [3]. Water splitting includes two semi-reactions, cathodic hydrogen evolution reaction (HER) and anodic oxygen evolution reaction (OER). Theoretically, 1.23 V of applied potential can split water into H<sub>2</sub> and O<sub>2</sub>. However, due to the influence of electrochemical reaction resistance, solution resistance, external circuit resistance, etc., the voltage applied at the two electrodes must be greater than 1.23 V. Therefore, it is necessary to use the electrocatalyst to reduce overpotential during the reaction process. Compared with the two-electron transfer kinetics HER process, the OER process is crucial for large-scale hydrogen production due to the four-electron transfer kinetics of OER on the anode electrode [4]. Therefore, it is necessary to

develop efficient, stable, and low-cost OER catalysts.

It is well known that noble metal-based catalysts exhibit good OER activity, but their high cost and scarcity limit their application. Thus, researchers have proposed different methods to prepare stable, active and low-cost electrocatalysts [5–7]. To achieve high OER performance, different methods including heteroatom doping, composition tuning, defect creation have been applied in the OER catalyst preparation. Transition metal sulfides based catalysts, e.g., MoS<sub>2</sub>@NiFe<sub>2</sub>O<sub>4</sub> [8], NiS/Fe<sub>3</sub>O<sub>4</sub> [9], Ni-Co-Fe-S/rGO [10], NiS-PBA/CNT [11], CoFe-C<sub>60</sub>FeS<sub>8</sub> [12], Co<sub>9</sub>FeS<sub>8</sub>/CoS [13], Ni/NiS heteronanoparticle-embedded semi-MOF [14], and Fe(OH)<sub>3</sub>/Ni<sub>9</sub>S<sub>8</sub> [15], have been used for the electrocatalysis of OER due to their rich content, low cost, and high activity. For example, NiS hollow microspheres have been proven to have good catalytic activity for OER [16]. The doping of Ni in Co<sub>0.85</sub>Se can improve the conductivity and OER activity [17]. Interestingly, recent reports indicate that Fe is also a potential candidate for the OER due to its environmentally friendly protocol and rich reserves [18]. However, compared with cobalt-based and nickel-based materials, iron-based materials have fewer active sites, leading to lower OER activity. Bell and his colleagues [19] found that Fe<sup>3+</sup> in Ni<sub>1-x</sub>Fe<sub>x</sub>OOH exhibited a

\* Corresponding authors.

E-mail addresses: [yinjieily@163.com](mailto:yinjieily@163.com) (J. Yin), [zhouhuawei@lcu.edu.cn](mailto:zhouhuawei@lcu.edu.cn) (H. Zhou), [kuoliu@ipe.ac.cn](mailto:kuoliu@ipe.ac.cn) (K. Liu).

short Fe-O bond distance, enabling OER intermediates to achieve near-optimal binding energy at the Fe position. The results show that Fe species, not Ni sites, are the active sites of OER. Among many iron-based sulfides, pyrite ( $\text{FeS}_2$ ) is a very rich sulfur mineral, which shows high reactivity in lithium-ion batteries, electrochemical glucose sensors, and photocatalysis [18]. Unfortunately,  $\text{FeS}_2$  without being doped by other elements mostly exhibited poor OER performance, as reported in the literature [20], and so far,  $\text{FeS}_2$  is unapplicable for OER. In our previous study [21], an amorphous/crystalline hybrid  $\text{FeS}_2$  supported on Ni foam (NF) catalyst was developed and exhibited an OER overpotential of  $\sim 190$  mV to deliver  $10 \text{ mA/cm}^2$  in  $1.0 \text{ M KOH}$ , indicating that by changing the structure of  $\text{FeS}_2$ , it is possible to improve the OER performance. However, the requirement of the special structure increased the complexity of preparation procedure. Until now, it is still a challenge to prepare the  $\text{FeS}_2$  catalyst with high OER performance.

The latest research results show that most of the electrocatalysts based on transition metal sulfides are OER pre-catalysts, rather than real "catalysts", because their composition, phase, and morphology will change dramatically, while these changes can further improve OER dynamics, especially in alkaline environments [22–25]. Zou et al. synthesized mackinawite  $\text{FeS}$  nanosheets on Fe foam, and found that transformation of  $\text{FeS}$  nanosheets to porous amorphous  $\text{FeO}_x$  film took place during OER [26]. Srinivas et al. prepared Ni/NiS heteronanoparticle-embedded semi-MOF nanosheets and applied them in water-splitting. Ni-OOH was found on the surface of Ni/NiS and acted as the active site during OER [14]. Nguyen et al. synthesized  $\text{FeNi-CoCrMnS}_2$  high entropy sulfide and self-reconstruction of the sulfides to metal (oxy)hydroxide was observed during OER [27]. However, identification of real active site on  $\text{FeS}_2$  is still rare and needs to be studied comprehensively.

In this paper, we designed  $\text{FeS}_2$  microspheres supported on Ni foam, which show excellent OER activity in alkaline electrolytes. At the current density of  $10 \text{ mA/cm}^2$ , its overpotential is  $170$  mV, which is superior to the commercial  $\text{RuO}_2$  catalyst, Ni foam, and most of the Fe-containing non-noble metal OER catalysts reported in the existing literature under the same test conditions (ranked top 4). The phase transition and the construction of the surface functional layer were investigated after OER.  $\text{FeS}_2$  microsphere reconstructed after OER, forming  $\text{FeS}_2@\text{FeOOH}$  microspheres with core-shell structure. The special structure increased oxidation state of iron species and  $\text{SO}_4^{2-}$ , promoting OER performances. This work provides solid evidence of the core-shell structure and important guiding information for designing efficient  $\text{FeS}_2$  containing OER catalysts.

## 2. Experimental section

### 2.1. Synthesis of pre-catalysts via microwave-assisted solvothermal method

$\text{FeS}_2$  pre-catalysts were synthesized via the microwave-assisted solvothermal method (Fig. S1).  $0.556 \text{ g}$  (2 mmol) of  $\text{FeSO}_4 \cdot 7 \text{ H}_2\text{O}$  and  $0.600 \text{ g}$  of polyvinyl pyrrolidone were dissolved in  $22 \text{ mL}$  ethylene glycol. Then  $0.128 \text{ g}$  (4 mmol) of sulfur powder was added. The solution was treated by ultrasound for 10 min before transferring to the microwave cavity operating at  $900 \text{ W}$  to be heated at  $200^\circ\text{C}$  for 1 h. After the process, the solution was allowed to cool down to room temperature. The precipitates were isolated by centrifuging, and washed with ethanol several times. Finally, the products were dried at  $60^\circ\text{C}$  under vacuum.

Homogeneous catalyst ink was obtained by sonication for 30 min, consisting of 3 mg of electrocatalyst,  $240 \mu\text{L}$  of ethanol,  $60 \mu\text{L}$  of Nafion solution (5 %), and  $300 \mu\text{L}$  of ethanol solution containing  $0.6 \text{ mg}$  of conductive carbon. The catalyst ink ( $100 \mu\text{L}$ ) was dropped on the pre-treated nickel foam ( $1 \text{ cm} \times 1 \text{ cm}$ ).

### 2.2. Electrochemical measurements

All electrochemical measurements were performed on an electrochemical workstation (Gamry 10010, USA) at temperature  $30^\circ\text{C}$  via a conventional three-electrode system in a  $1.0 \text{ M KOH}$  electrolyte. The working electrode is nickel foam ( $1 \text{ cm} \times 1 \text{ cm}$ ) coated with the catalyst, the reference electrode is  $\text{Hg/HgO}$ , and the counter electrode is a graphite rod electrode. All potentials measured were calibrated to reversible hydrogen electrode (RHE) using the equation [28]:

$$E_{\text{vs.RHE}} = E_{\text{vs.Hg/HgO}} + 0.059 \times \text{pH} + 0.098$$

Polarization curves of linear sweep voltammetry (LSV) were acquired at a scan rate of  $5.0 \text{ mV/s}$  from  $0 \text{ V}$  to  $1 \text{ V}$  via the  $\text{Hg/HgO}$  reference electrode. The iR manual compensation (with a compensation level of 90 %) was applied to all polarization curves to eliminate ohmic resistance in the measurement system including solution and conductive wire. Cyclic voltammetry (CV) curves were measured within the non-Faradaic regions at different scanning rates ( $20, 40, 60, 80$ , and  $100 \text{ mV/s}$ ). Electrochemical impedance spectroscopy (EIS) was conducted with the frequency range of  $100 \text{ kHz}$  to  $0.1 \text{ Hz}$  with an alternating current (AC) voltage of  $10 \text{ mV}$  and direct current (DC) voltage of  $0.6 \text{ V}$  vs  $\text{Hg/HgO}$  reference electrode.

### 2.3. Materials characterization

Morphological and structural characterization, energy-dispersive X-ray spectroscopy (EDS), and element mapping of catalysts were performed using scanning electron microscopy (SEM) on a Thermo Fisher Scientific FIB-SEM GX4 and the JEM-2100 transmission electron microscope (TEM) made by JEOL Ltd., Japan. X-ray photoelectron spectroscopy (XPS) was recorded on a Thermo ESCALAB 250. X-ray diffraction (XRD) data of samples was collected using PAN analytical X'Pert diffractometer ( $\text{Cu-K}\alpha$  radiation at  $\lambda = 1.54 \text{ \AA}$ ) sampling at  $6^\circ/\text{min}$ ,  $40 \text{ KeV}$ , and  $100 \text{ mA}$ . Raman spectra before and after OER were collected using a Renishaw inVia Raman spectrometer with the laser wavelength at  $633 \text{ nm}$  at room temperature.

### 2.4. iR-calibration and overpotential

In the electrolytic cell, charge transfer resistance, intrinsic resistance and contact resistance will lead to electric energy consumption. Thus, the overpotential compensated by iR is more important than that without iR compensation.

iR compensation for OER can be described as [29]:

$$\eta_{\text{OER}} = E_{\text{vs.RHE}} - 1.23 - E_{\text{iR}}$$

where  $\eta_{\text{OER}}$  is the overpotential for OER at a particular current density,  $E_{\text{vs.RHE}}$  is the measured potential vs. RHE, and  $E_{\text{iR}}$  represents the iR compensated overpotential.

### 2.5. Active area calculation

In the typical "capacitance" method, cyclic voltammetry (CV) is performed in a small potential window (normally  $\pm 50 \text{ mV}$  around the open-circuit potential (OCP)) in which non-Faradaic processes occur. Half of the current difference ( $\Delta I/2$ ) between the anodic current ( $I_a$ ) and the cathodic current ( $I_c$ ) at the centered potential is obtained and plotted against the scan rate ( $v$ ) to fit a straight line with the slope value of  $C_{\text{dl}}$ . The slope is the capacitance.

## 3. Results and discussion

### 3.1. Activity of OER

As shown in Fig. S1,  $\text{FeS}_2$  microspheres were synthesized by the

simple microwave-assisted solvothermal method. The formation mechanism of  $\text{FeS}_2$  microspheres is as follows: (1)  $2\text{CH}_2\text{OH} \rightarrow \text{CH}_3\text{COCOCH}_3 + \text{S}^{2-} + 2\text{H}^+ + 2\text{H}_2\text{O}$ ; (2)  $(\text{n}-1)\text{S} + \text{S}^{2-} \rightarrow \text{S}_n^{2-}$ ; (3)  $\text{Fe}^{2+} + \text{S}_n^{2-} + \text{S}^{2-} \rightarrow \text{FeS}_2 + \text{S}_n^{2-}$  [30]. X-ray diffraction (XRD) results of the prepared sample show the crystal planes of  $\text{FeS}_2$  (PDF#71-0053, Fig. S2a). SEM images of  $\text{FeS}_2$  microspheres are shown in Fig. 1a-c. The microspheres prepared by microwave are uniform, and the average particle size is  $2.39\text{ }\mu\text{m}$  (Fig. S2b). Based on XRD and SEM results,  $\text{FeS}_2$  microspheres with an average diameter of  $2.39\text{ }\mu\text{m}$  were successfully

synthesized.

The performance of  $\text{FeS}_2$  microspheres (MS) supported on NF ( $\text{FeS}_2$  MS/NF) was evaluated in a standard three-electrode system. All LSV curves and subsequent electrochemical curves are obtained after repeated scanning of CV for many times until all curves are stable, which ensures complete phase transition and the construction of functional layers. The compensated curve shows that the OER performance of  $\text{FeS}_2$  MS/NF is better than that of commercial  $\text{RuO}_2$  and blank Ni foam (NF) (Fig. 1d).  $\text{FeS}_2$  MS/NF demands an overpotential of  $170\text{ mV}$  to afford a

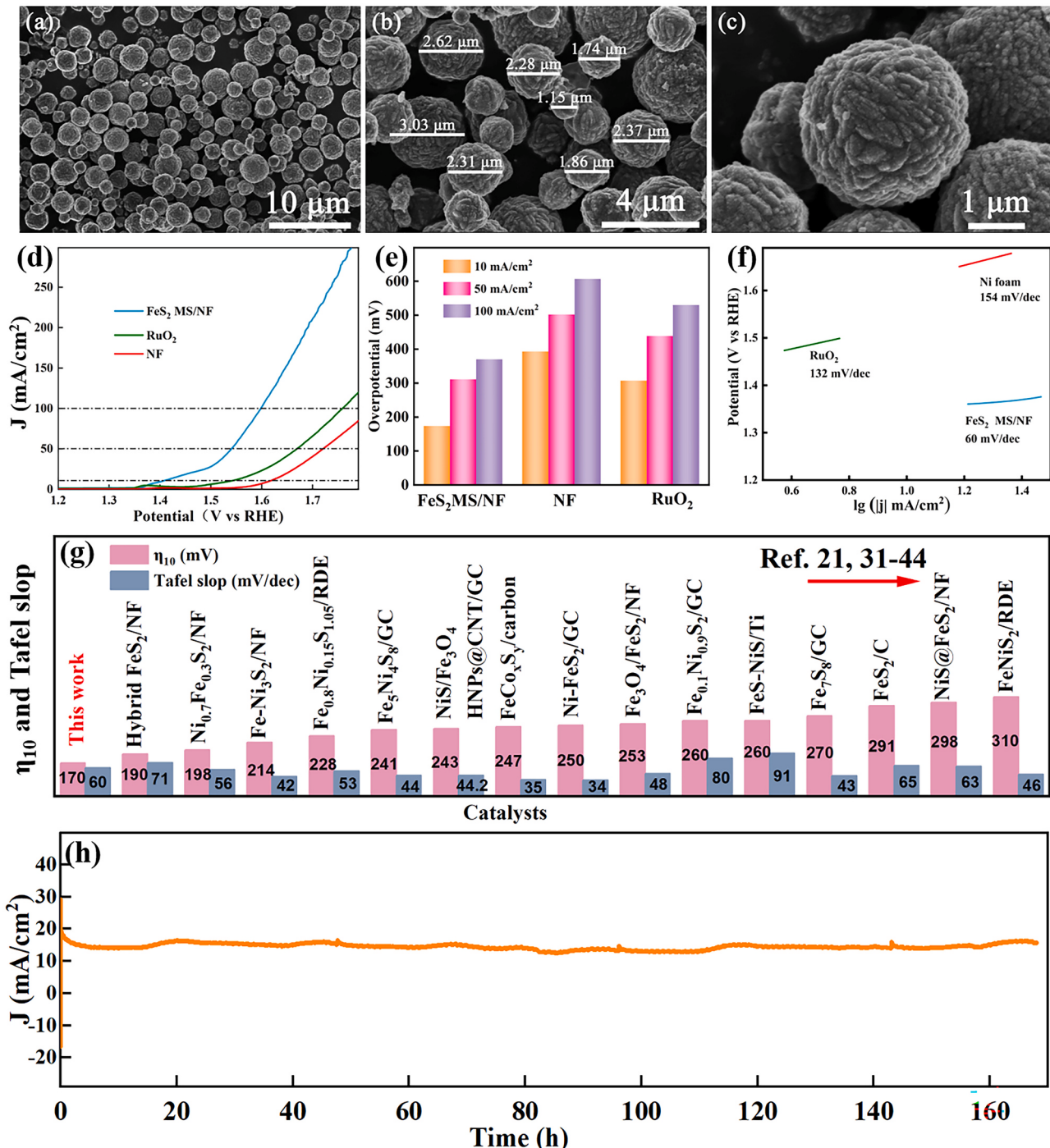


**Fig. 1.** (a-c) SEM images of  $\text{FeS}_2$  microspheres; (d) Linear sweep voltammetry (LSV); (e) Overpotentials at current densities of  $10$ ,  $50$ , and  $100\text{ mA}/\text{cm}^2$ ; (f) Tafel plots; (g) Comparison of OER activities between  $\text{FeS}_2$  microspheres/Ni foam ( $\text{FeS}_2$  MS/NF) in this work and some state-of-the-art Fe/S-based OER electrodes in alkaline media from previous reports under the same test conditions [21,31–44]. (h) Chronoamperometric measurement under a constant potential of  $0.6\text{ V}$  versus reference electrode.  $J$  and  $j$ : current density;  $\eta_{10}$ : the overpotential at  $10\text{ mA}/\text{cm}^2$ .

current density of  $10 \text{ mA/cm}^2$  less than that for  $\text{RuO}_2$  (301.5 mV) and Ni foam (387.5 mV) in 1.0 M KOH, as shown in Fig. 1e. When the current densities are 50 and  $100 \text{ mA/cm}^2$ , the overpotentials are 283 and 314 mV respectively, showing the performance of  $\text{FeS}_2$  MS/NF is much better than the electrocatalytic performance of  $\text{RuO}_2$  ( $405.9 \text{ mV}$  at  $50 \text{ mA/cm}^2$ ,  $462.8 \text{ mV}$  at  $100 \text{ mA/cm}^2$ ). The Tafel slope is an important index to evaluate electrochemical activity, which is usually obtained from the linear part of Tafel plots at high overpotential. The number of active centers, the charge transfer efficiency, and the free energy of hydrogen on the surface of the electrocatalyst all affect the Tafel slope. As shown in Fig. 1f, the Tafel slope of  $\text{FeS}_2$  MS/NF is  $60 \text{ mV/decade}$ , which is significantly lower than  $\text{RuO}_2$  ( $132 \text{ mV/decade}$ ) and Ni foam ( $154 \text{ mV/decade}$ ), indicating that  $\text{FeS}_2$  MS/NF possesses faster electron transfer, thereby significantly improving the catalytic activity of OER. Furthermore, by comparing the performance of  $\text{FeS}_2$  MS/NF with the catalysts reported in other literatures [21,31–44] (Fig. 1g and Table S1), it is found that the performance of this simple  $\text{FeS}_2$  MS/NF catalyst in the alkaline electrolyte is more excellent (ranked top 4) than most of the Fe- and S-containing non-noble metal catalysts reported in the existing literatures, e.g.,  $\text{FeOOH}$  nanoparticles/Fe-Ni LDH/carbon disk ( $174 \text{ mV}$  at  $10 \text{ mA/cm}^2$ ) [45], core-shell  $\text{NiFeCu}/\text{NF}$  ( $180 \text{ mV}$  at  $10 \text{ mA/cm}^2$ ) [46],  $\text{Ni}_x\text{Fe}_{3-x}\text{O}_4$ -EDTA/NF ( $180 \text{ mV}$  at  $10 \text{ mA/cm}^2$ ) [47],  $\text{Ni}_{0.7}\text{Fe}_{0.3}\text{S}_2/\text{NF}$  ( $198 \text{ mV}$  at  $10 \text{ mA/cm}^2$ ) [31],  $\text{Fe-Ni}_3\text{S}_2/\text{NF}$  ( $214 \text{ mV}$  at  $10 \text{ mA/cm}^2$ ) [32], and a  $\text{FeS}_2$  nanohybrid catalyst on NF developed recently by our group ( $\sim 190 \text{ mV}$  at  $10 \text{ mA/cm}^2$ ) [21]. The overpotentials ( $\eta$ ) on phosphorus-rich phosphorus-accumulating organisms assisted P-functionalized  $\text{Ni}_{20}\text{Fe}_1$  on NF (PR-PAOs- $\text{Ni}_{20}\text{Fe}_1/\text{NF}$ ) ( $137 \text{ mV}$  at  $10 \text{ mA/cm}^2$ ) [48],  $\text{FeP}/\text{Ni}_2\text{P}/\text{NF}$  ( $154 \text{ mV}$  at  $10 \text{ mA/cm}^2$ ) [49], and  $(\text{NiFe})\text{OOH}/\text{NF}$  ( $154 \text{ mV}$  at  $10 \text{ mA/cm}^2$ ) [50] are lower, but  $\text{FeS}_2$  MS/NF with higher  $\eta$  value have the advantages of simple preparation method and structure. Through clarifying the property of  $\text{FeS}_2$  microspheres, it is possible to help understanding the working principles of  $\text{FeS}_2$  in the alkaline electrolyte. In order to evaluate the stability of the catalyst, the prepared  $\text{FeS}_2$  electrode was tested for 170 h under a constant potential of 0.6 V versus reference electrode by the

chronoamperometric measurements. The test results are shown in Fig. 1h. Within 170 h, the overpotential basically remains unchanged, indicating that the  $\text{FeS}_2$  MS/NF have outstanding stability for water oxidation reaction under alkaline conditions.

A water-splitting device was fabricated by using  $\text{FeS}_2$  MS/NF as an anode and Pt/C/NF as a cathode in 1.0 M KOH electrolyte. As shown in Fig. 2a, the double electrode system of  $\text{FeS}_2$  MS/NF as an anode and Pt/C/NF as a cathode shows lower potential and better OER catalytic performance than that based on  $\text{RuO}_2/\text{NF}$  as an anode and Pt/C/NF as a cathode and NF as an anode and NF as a cathode. The potential is only  $1.448 \text{ V}$  at the current density of  $10 \text{ mA/cm}^2$  (Fig. 2b), which is lower than those on the S-containing OER catalysts in the literature [34,41]. This suggests that application of  $\text{FeS}_2$  MS/NF as an anode and Pt/C/NF as a cathode improves the catalytic activity of overall water splitting. According to the chronoamperometry result (Fig. 2c), the stability test operating at a constant voltage of 1.6 V shows that the current hardly decreases within 5 h, indicating that  $\text{FeS}_2$  MS/NF as an anode has good catalytic stability for overall water splitting.

Temperature is another important factor affecting the electrochemical reaction rate. For most reactions, the higher the temperature, the faster the reaction rate. Here, we tested the performance of catalysts at different temperatures. With the increase of temperature,  $\text{FeS}_2$  MS/NF exhibited much higher OER activity (Fig. 3a). The excellent linearity between potential and  $\lg |j|$  in Fig. S3 demonstrates that the charge transfer at the interface of solution/catalyst is the rate-determining step at different temperatures [51]. The operating temperature of electrolytic cell in industrial production was commonly used at  $60\text{--}80^\circ\text{C}$  [52,53]. Therefore, the results at  $60^\circ\text{C}$  and  $80^\circ\text{C}$  were analysed in detail. At  $60^\circ\text{C}$ ,  $\text{FeS}_2$  MS/NF exhibited low overpotentials of 166, 260, and 282 mV at current densities of 10, 50, and  $100 \text{ mA/cm}^2$ , respectively, during the LSV test (Fig. 3b). At  $80^\circ\text{C}$ ,  $\text{FeS}_2$  MS/NF exhibited low overpotentials of 158, 236, and 255 mV at current densities of 10, 50, and  $100 \text{ mA/cm}^2$ , respectively (Fig. 3b). Finally, a water splitting device was fabricated by two-electrode system in 1.0 M KOH. The water splitting experiment was carried out at different temperatures. As shown

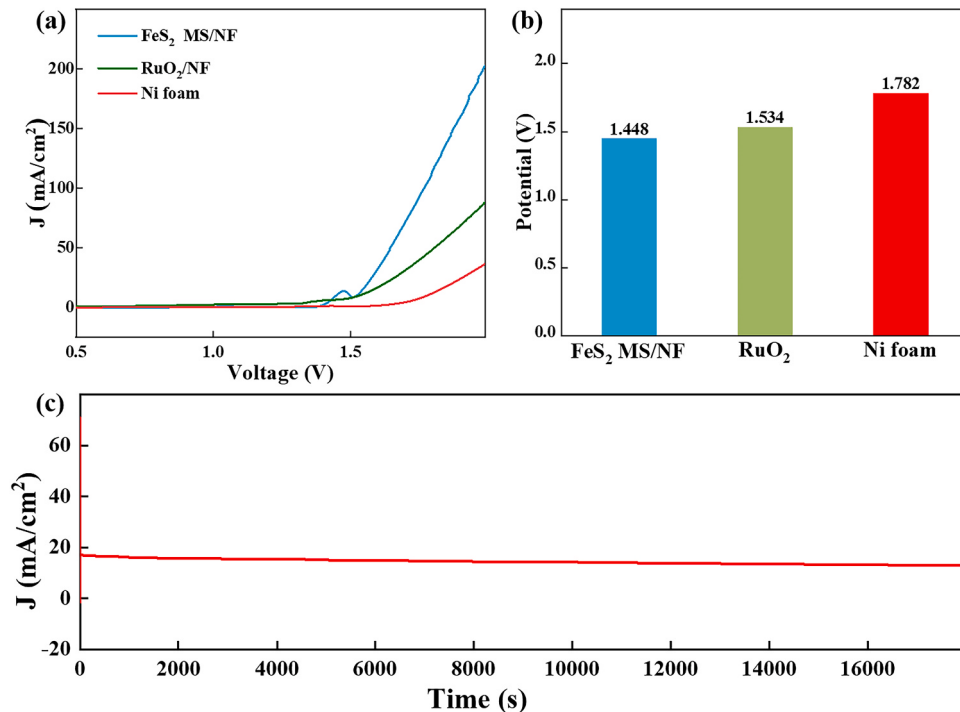


**Fig. 2.** (a) LSV and (b) potentials at current density of  $10 \text{ mA/cm}^2$  for the systems of  $\text{FeS}_2$  MS/NF as an anode and Pt/C/NF as a cathode,  $\text{RuO}_2/\text{NF}$  as an anode and Pt/C/NF as a cathode, and Ni foam as an anode and Ni foam as a cathode. (c) Chronoamperometric measurement of the system of  $\text{FeS}_2$  MS/NF as an anode and Pt/C/NF as a cathode under a constant potential of 1.6 V.

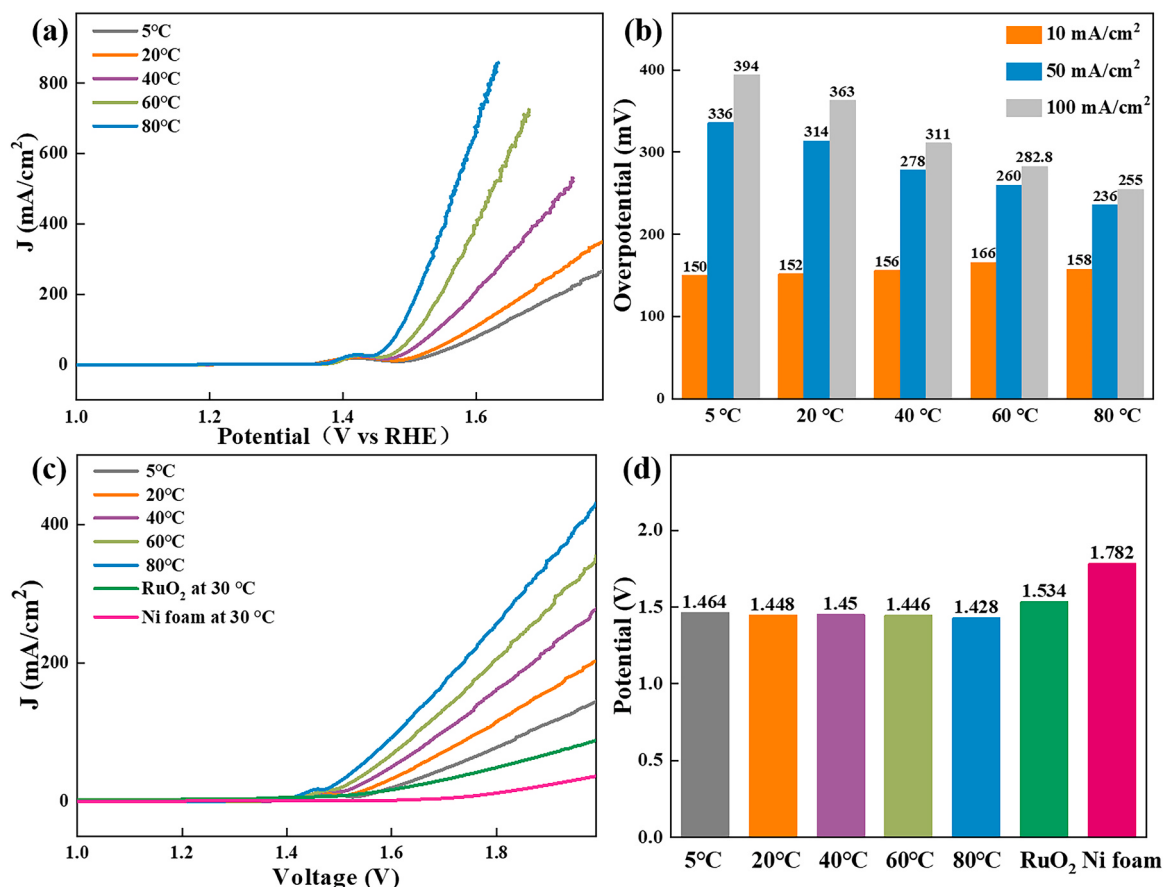


**Fig. 3.** (a) LSV and (b) overpotentials at current densities of 10, 50, 100 mA/cm<sup>2</sup> for FeS<sub>2</sub> MS/NF. (c) LSV and (d) potentials at current density of 10 mA/cm<sup>2</sup> for the double electrode systems of FeS<sub>2</sub> MS/NF as an anode and Pt/C/NF as a cathode, RuO<sub>2</sub>/NF as an anode and Pt/C/NF as a cathode, and Ni foam as an anode and Ni foam as a cathode at different temperatures.

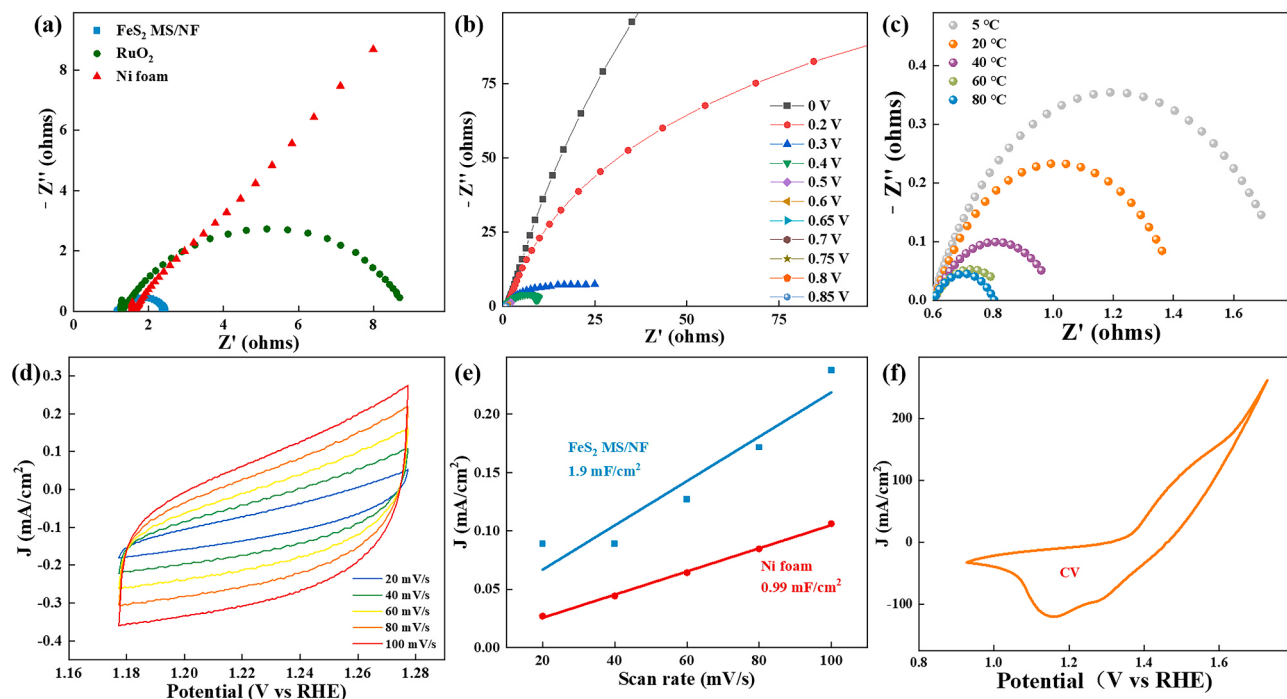


**Fig. 4.** Nyquist plots of (a) FeS<sub>2</sub> MS/NF, RuO<sub>2</sub>, and bare Ni foam in 1.0 M KOH, (b) FeS<sub>2</sub> MS/NF at different potentials versus RHE, and (c) FeS<sub>2</sub> MS/NF at different temperatures. (d) Cyclic voltammetry curves of FeS<sub>2</sub> MS/NF measured within the non-Faradaic regions. (e) Plots of current density versus voltage scan rate of FeS<sub>2</sub> MS/NF and bare Ni foam in 1.0 M KOH. (f) CV curve of FeS<sub>2</sub> MS/NF with a 100 mV/s scan rate from 0.8 to 1.8 V<sub>RHE</sub> (vs. RHE).

in Fig. 3c and d, the activity is improved at a higher temperature (60 °C), and a lower voltage (1.446 V) is required to provide the same current density of 10 mA/cm<sup>2</sup>. When the temperature increases to 80 °C, only 1.428 V is required at the current density of 10 mA/cm<sup>2</sup>. In addition, LSV in Fig. 3 has a bulge, similar to the LSV for FeS<sub>2</sub> MS/NF in Fig. 1. It was reported that surface metal Ni and oxides (Ni<sup>2+</sup>) formed oxides/s/hydroxyl radicals (Ni<sup>3+</sup>) before the generation of oxygen, producing Ni(OH)<sub>x</sub>, NiO<sub>x</sub>, NiOOH and other substances on the surface of Ni foam, and thus, the oxidation current appears [54–56]. Similarly, contribution of FeS<sub>2</sub> MS oxidation to the bulge in Fig. 3 cannot be excluded. The results above indicate that oxidation of both FeS<sub>2</sub> and NF might take place.

To further understand the evaluated kinetics and mass transport between the catalyst and electrolyte, EIS was conducted. As shown in the Nyquist diagram (Fig. 4a) and the fitting results (Table S2), the charge transfer resistance of FeS<sub>2</sub> MS/NF is only 0.81 Ω, much smaller than that of RuO<sub>2</sub> (9.97 Ω) or Ni foam (13.74 Ω), which means faster OER kinetics

and better surface electron transfer. Furthermore, EIS at different potentials were conducted to explore the electrocatalytic OER kinetics (Fig. 4b-c and Tables S3–S4). It could be observed that with the increase of voltage or temperature, the charge transfer resistance of FeS<sub>2</sub> MS/NF changes from large to small, indicative of the faster electron transfer. It should be noted that at 0.5 V relative to the reference electrode Hg/HgO, the charge transfer resistance of FeS<sub>2</sub> MS/NF underwent a sudden decrease, indicating that OER occurred. Considering that the electrochemical active surface area (ECSA) will affect the catalytic performance of OER, we deduced the electrochemical double capacitance ( $C_{dl}$ , Fig. 4e) from the CV curves (Fig. 4d and S4) to further estimate the ECSA of the catalyst. Remarkably, the  $C_{dl}$  of FeS<sub>2</sub> MS/NF (1.9 mF/cm<sup>2</sup>) is higher than that of 0.99 mF/cm<sup>2</sup> for Ni foam, which indicates that FeS<sub>2</sub> MS/NF exposes abundant active sites. Therefore, FeS<sub>2</sub> MS/NF exhibited fast electron transfer and abundant active sites, leading to the high OER activity. Fig. 4f shows cyclic voltammogram (CV) with typical features of Fe-based electrocatalysts due to redox transitions of the Fe<sup>3+</sup>–Fe<sup>2+</sup>.

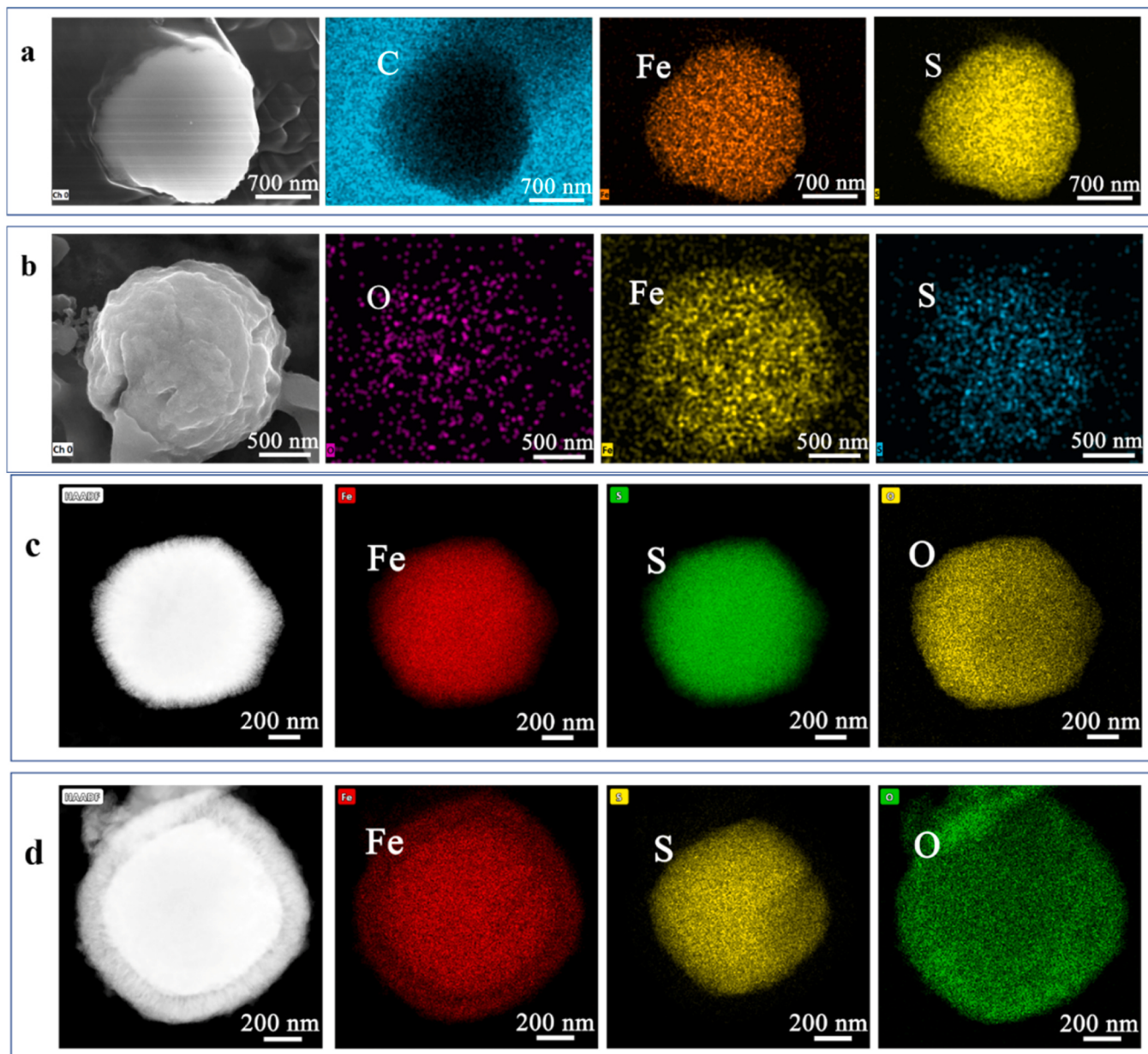


**Fig. 5.** SEM images and elemental mapping of (a) fresh FeS<sub>2</sub> MS and (b) FeS<sub>2</sub> MS after OER. HAADF-STEM image and elemental mapping of (c) fresh FeS<sub>2</sub> MS and (d) FeS<sub>2</sub> MS after OER.

The redox transition CV curve of the catalyst shows a broad redox transition peak at  $\sim 1.42$  V<sub>RHE</sub> (vs. RHE) [42]. The redox peak coincides with the onset of the OER and suggests the self-reconstruction of the FeS<sub>2</sub> microspheres under reaction conditions. The following section focused on clarifying the structure change and the intrinsic active species of the FeS<sub>2</sub> microspheres after OER.

### 3.2. Reconstruction of FeS<sub>2</sub> microspheres during OER process

To investigate the reconstructed functional structure of FeS<sub>2</sub> microspheres for enhancing the electrocatalytic OER activity and stability, a series of structural characteristics were carried out. To observe the internal structure of the microsphere, the microsphere was cut via the method of focused ion beam (Fig. S5). The cross-section image of the microsphere is shown in Fig. 5a. The microsphere is a solid structure, and the elements Fe and S are evenly distributed (EDS images, Fig. 5a). After OER reaction, the unique microsphere structure of FeS<sub>2</sub> MS remains unchanged (Fig. 5b), and the O element can be clearly detected, indicating that oxidized Fe species appeared. To investigate the change of the structure, high-angle annular dark field scanning transmission electron microscopic images (HADDF-STEM) were collected for fresh and used FeS<sub>2</sub> microspheres. The fresh FeS<sub>2</sub> MS is microsphere (Fig. 5c). After OER, a thick shell is found on the surface of the catalyst (Fig. 5d), indicating that the core-shell structure of the FeS<sub>2</sub> microsphere catalyst was constructed after OER reaction. The information on element distribution obtained from TEM-EDS is consistent with SEM (Fig. 5), which also proves the uniform distribution of Fe, S, and O elements. Obviously, as shown in Fig. 5c-d, the content of S element in the shell is severely reduced after OER, but the O element is obviously increased. The area occupied by Fe or O element exceeds that occupied by S after OER, proving that the fresh FeS<sub>2</sub> microspheres undergoes surface reconstruction, and iron oxides or other kinds of oxidized Fe species are proposed to form on the surface of the FeS<sub>2</sub> microspheres.

The microsphere was further characterized by high-resolution TEM (HRTEM). Fig. 6a and f displays the morphology of the catalyst before and after OER. As shown in Fig. 6b, the corresponding selected area electron diffraction (SAED) images obtained from the edge of the microsphere reveal the (111), (210), and (311) crystal planes of FeS<sub>2</sub> (PDF#71-0053). The bright and recognizable spots indicate that the microsphere is highly crystalline. Consistent with SEM, there are a lot of protrusions on the surface of microspheres (Fig. 6c). Enlarge the rectangular area in Fig. 6d, and the clear lattice stripes also indicate the high crystallinity of the microspheres. The 0.22 nm crystal plane spacing belongs to the (211) atomic plane of FeS<sub>2</sub> (Fig. 6e). In contrast, the

widely diffused halo rings (Fig. 6g) and HRTEM in the activated SAED suggest the amorphous nature of the catalyst. The thickness of the shells is about 152 nm as shown in Fig. 6h. In addition, when the rectangular area in Fig. 6i was enlarged, a large number of defects and disordered structures (purple circle marks) appear, which may be oxidized iron, Fe (OH)<sub>3</sub> or FeOOH caused by surface reconstruction (Fig. 6j). According to the XRD results of the crystal structure and composition of the microspheres before and after reaction (Fig. 7a), the catalyst after OER did not show any new diffraction peaks compared with the pre-catalyst, indicating the amorphous nature of the reconstructed layer, consistent with the absence of any typical lattice fringes under HRTEM and the widespread halo ring in SAED (Fig. 6). The concentration of S species in the shell of FeS<sub>2</sub> MS decreases (Fig. 5c-d) after OER, possibly due to S leaching, forming amorphous shell. Therefore, it is possible that the lattice defects include S vacancies formed by S leaching. The amorphous lattice defects may optimize the adsorption energy of the catalyst for oxygen and water so that it has excellent OER performance [57,58].

To better understand the chemical state and element composition of the microsphere surface, X-ray photoelectron spectroscopy (XPS) measurements were carried out. Comparing the peaks in the Fe 2p region before and after reaction, the peaks at 706.8 and 719.4 eV before reaction belong to Fe(II)-S, and the peaks at 711.5 and 724.8 eV could be assigned to Fe(III)-O, which may be caused by surface oxidation when exposed to air. After reaction, the peaks in the Fe 2p region changed greatly (Fig. 7b). The peaks with binding energies of 712.3 and 726.5 eV belong to Fe<sup>3+</sup>2p<sub>3/2</sub> and Fe<sup>3+</sup>2p<sub>1/2</sub>, respectively, indicative of the Fe<sup>3+</sup> species possibly from Fe<sub>2</sub>O<sub>3</sub>, FeOOH or Fe(OH)<sub>3</sub>. The satellite peak at 717.5 eV (identified as "Sat.") proves the existence of FeOOH [59]. In addition, in the O 1s region (Fig. 7c), it is observed that after OER reaction, three main peaks at 532, 533 and 536 eV corresponding to Fe-O-Fe bond, Fe-O-H bond, and H-O-H bond appeared. No peak at 530 eV was observed, indicative of the absence of Fe<sub>2</sub>O<sub>3</sub>. The presence of surface -OH groups demonstrates that oxidized iron species may be FeOOH or Fe(OH)<sub>3</sub>. In order to identify the Fe species, Raman spectra were collected before and after reaction (Fig. 7d). Before the OER reaction, the characteristic peaks at 337 cm<sup>-1</sup> and 370 cm<sup>-1</sup> corresponding to the values of the Eg and Ag modes of pyrite FeS<sub>2</sub> [20] were observed (Fig. 7d), indicating that the catalyst was composed of FeS<sub>2</sub>. After OER reaction, a characteristic peak of FeOOH (575.7–678.8 cm<sup>-1</sup>) appeared [60], suggesting that FeOOH formed during the OER reaction. The peaks attributed to Fe<sub>2</sub>O<sub>3</sub>, Fe<sub>3</sub>O<sub>4</sub> or other kinds of Fe species were not observed in the Raman results, indicating that the FeOOH covered the surface of FeS<sub>2</sub> after OER reaction. It is believed that the increased oxidation state of transition metals with higher valence state is helpful to

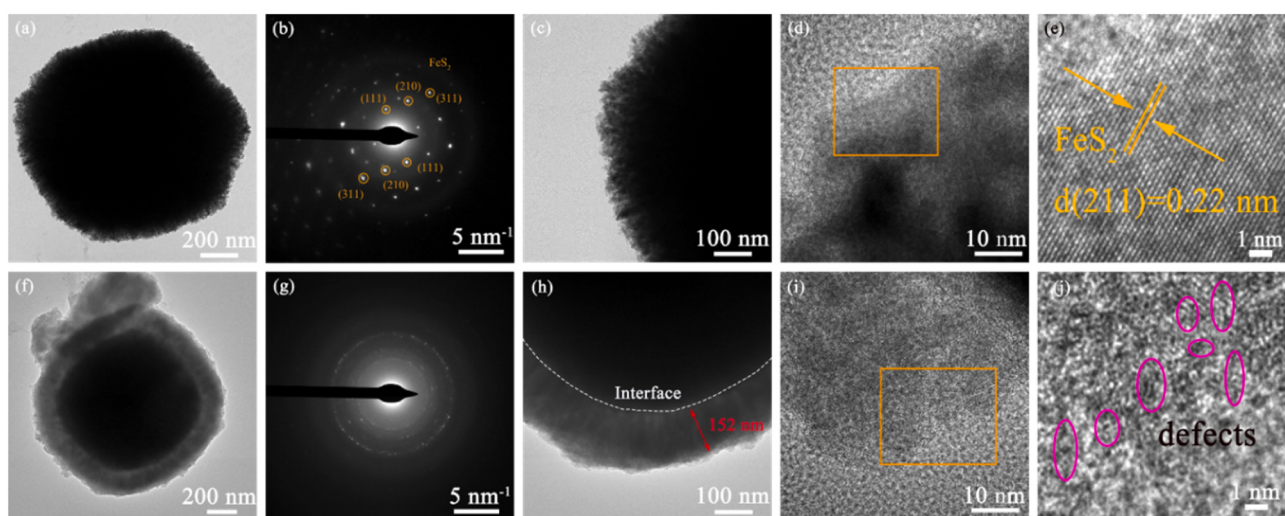
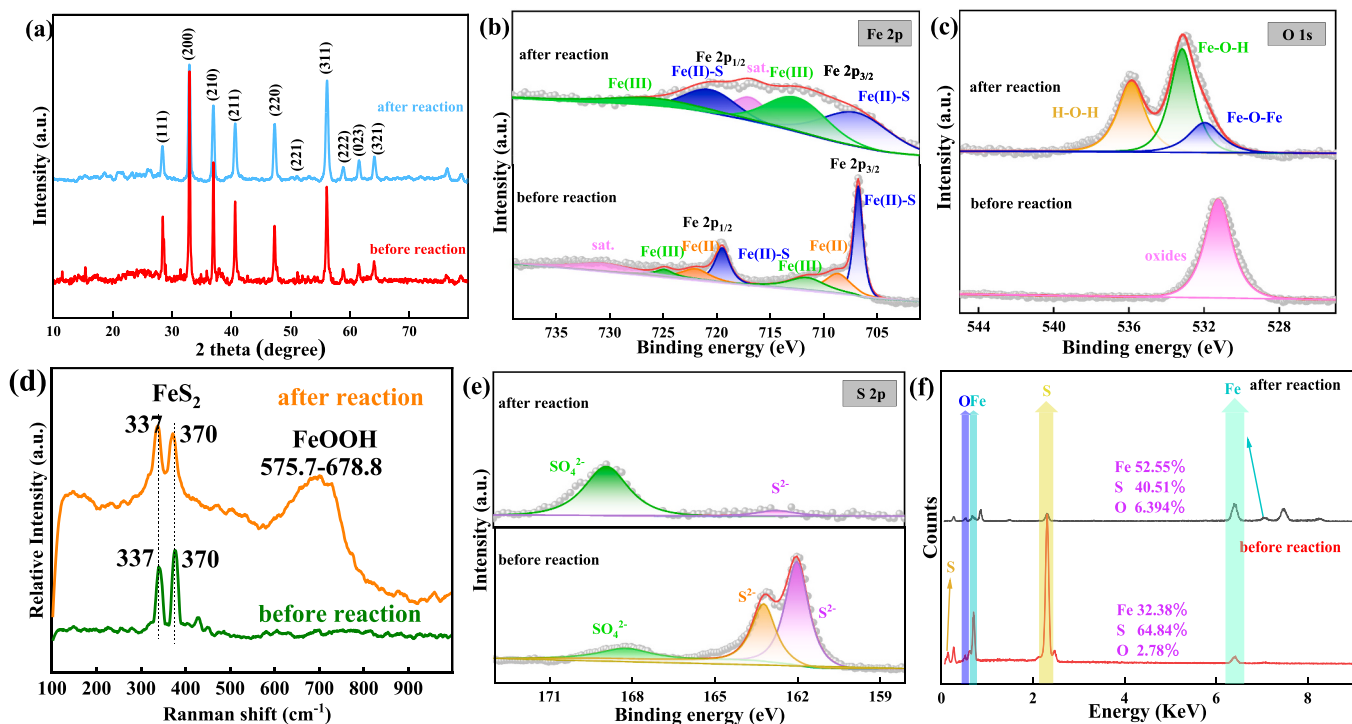
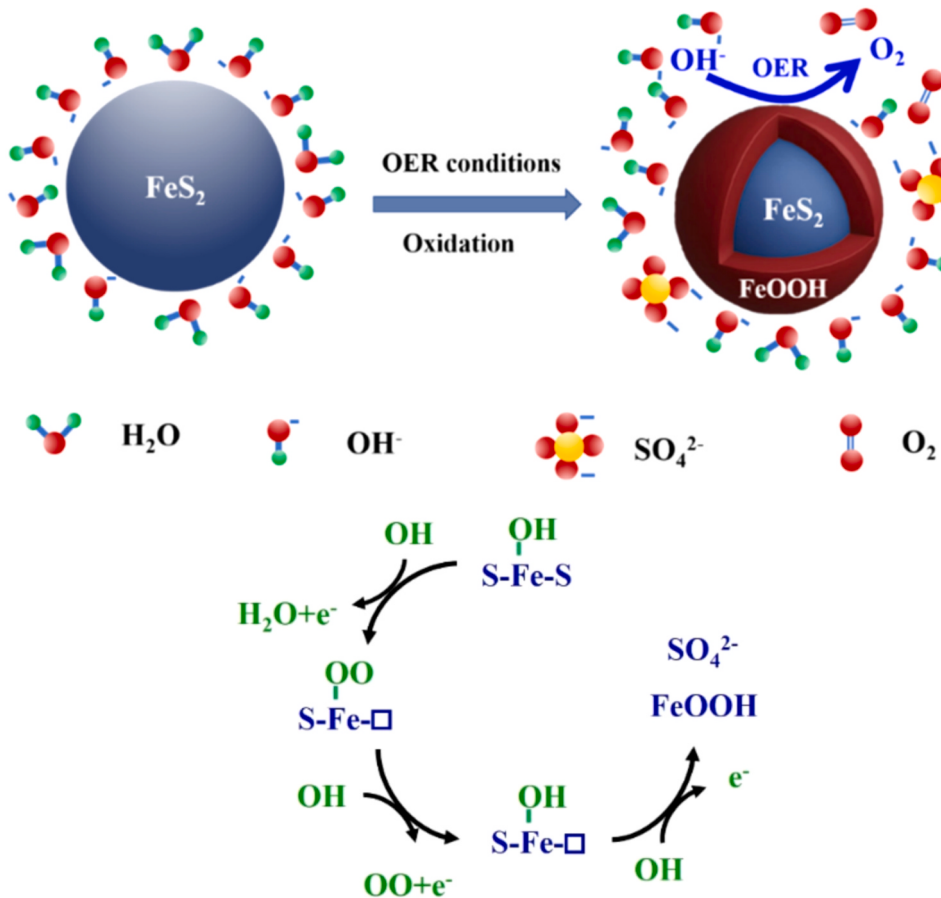


Fig. 6. TEM images of (a-e) fresh FeS<sub>2</sub> MS and (f-j) FeS<sub>2</sub> MS after OER. (b, g) SAED patterns and (e, j) high-resolution TEM images.



**Fig. 7.** (a) XRD patterns, (b) Fe 2p XPS spectra, (c) O 1s XPS spectra, (d) Raman spectra, and (e) S 2p XPS spectra of FeS<sub>2</sub> MS before and after reaction. (f) The percentage of Fe, S, and O elements in FeS<sub>2</sub> MS before and after reaction according to elemental analysis based on SEM.



**Fig. 8.** Surface reconstruction of FeS<sub>2</sub> MS to FeS<sub>2</sub>@FeOOH and proposed formation process of FeOOH shell during OER.

participate in the multi-electron transport process of water oxidation [61], which may be one of the reasons why the catalyst has excellent OER performance.

The change of S species during OER reaction was also investigated. In the 2p energy spectrum of S (Fig. 7e), the peaks of binding energy at 162 and 163.2 eV belong to  $S^{2-}$  in  $FeS_2$ , and the peak at 168.2 eV corresponds to  $SO_4^{2-}$  caused by surface oxidation. After reaction, characteristic peaks of  $S^{2-}$  reduced dramatically and were even negligible in comparison with the peaks before reaction, while the peaks of  $SO_4^{2-}$  increased, indicating the transform of sulfide to oxides during OER reaction (Fig. 7e). As shown in Fig. 7f, the content of S decreased dramatically after reaction, consistent with HADDF-STEM results (Fig. 5c-d), indicating that S leaching took place and S species was oxidized to  $SO_4^{2-}$  [62]. The above shows that electrochemical OER reaction can oxidize sulfur and transition metals [63]. According to the literature [64], the residual  $SO_4^{2-}$  adsorbed on surface can stabilize the intermediate of  $OOH^*$ , and thus enhance the OER performances. It should be noted that S leaching could result in sulfur vacancies on the amorphous shell, possibly beneficial for  $H_2O$  adsorption and electronic conductivity, leading to the high OER activity [65–68].  $FeS_2$  microspheres lose a lot of sulfur after OER reaction, forming a layer of amorphous  $FeOOH$  shell, which is different from traditional iron oxides. This unique core-shell structure is naturally formed in the process of OER reaction or the electric activation and shows excellent OER performance.

Above all, we speculated a reaction scheme for surface reconstruction of  $FeS_2$  microspheres to form the  $FeS_2@FeOOH$  core-shell structure (Fig. 8). During the OER reaction, a large amount of sulfur is dissolved from the surface of  $FeS_2$  microspheres to form a layer of amorphous  $FeOOH$  shell. Similar to  $Ni_3S_2/NF$  reported by Wu et al. [62], it is possible that the S leaching takes place in combination with  $OH^-$  adsorption followed by electron transfer, leading to the formation of  $FeOOH$  shell and  $SO_4^{2-}$ . S leaching promotes the electrochemical structure reconstruction of  $FeS_2$  microspheres to form core-shell  $FeS_2@FeOOH$ . The inner core of the microspheres still maintains the  $FeS_2$  crystal phase, while the dissolved sulfur forms  $SO_4^{2-}$  under the OER conditions. This special structure may optimize the adsorption energy of the catalyst for water and oxygen, so that it has excellent electrocatalytic oxygen evolution performance.

#### 4. Conclusions

In conclusion, we designed and prepared  $FeS_2$  MS/NF as OER catalyst. Through a series of structural characterization and analysis, it is confirmed that after OER, the sulfur on the surface of the microspheres largely dissolved and a shell of amorphous  $FeOOH$  is formed, while the internal core still maintained the crystal phase of iron disulfide. This unique core-shell structure makes the catalyst more conductive than traditional  $FeOOH$  and  $FeS_2$ , and the amorphous shell and a large number of lattice defects may optimize the adsorption energy of the catalyst for water and oxygen to enhance OER performance. The increased oxidation state of iron species from  $FeS_2$  to  $FeOOH$  promotes the multi-electron transport process of water oxidation, and  $SO_4^{2-}$  formed from S leaching combined with  $OH^-$  adsorption can stabilize the intermediate of  $OOH^*$ , beneficial for OER. At the current density of 10 mA/cm<sup>2</sup>, the overpotential is only 170 mV, a better performance than those on the Fe/S-based non-noble metal catalysts in the existing literature. This research provides an effective strategy for designing OER catalyst via self-optimizing reconfiguration of functional layer and advances the development of electrolytic water technology.

#### CRediT authorship contribution statement

**Caizhen Yue:** Investigation, Data curation, Writing – original draft. **Xuena Zhang:** Data curation. **Jie Yin:** Conceptualization, Funding acquisition, Supervision, Writing – review & editing. **Huawei Zhou:** Investigation, Writing – review & editing. **Kuo Liu:** Conceptualization,

Formal analysis, Supervision, Writing – review & editing. **Xin Liu:** Investigation, Funding acquisition.

#### Declaration of Competing Interest

The authors declare that they have no known competing financial interests or personal relationships that could have appeared to influence the work reported in this paper.

#### Data availability

Data will be made available on request.

#### Acknowledgements

This work was financially supported by the Shandong Province Natural Science Foundation (Grant No. ZR2019MB021), the Natural Science Foundation of Hebei Province (Grant No. A2021501007), and the National Natural Science Foundation of China (Grant No. 11775226).

#### Appendix A. Supporting information

Supplementary data associated with this article can be found in the online version at [doi:10.1016/j.apcatb.2023.123171](https://doi.org/10.1016/j.apcatb.2023.123171).

#### References

- [1] M.S. Dresselhaus, I.L. Thomas, Alternative energy technologies, *Nature* 414 (2001) 332–337.
- [2] G.W. Crabtree, M.S. Dresselhaus, M.V. Buchanan, The hydrogen economy, *Phys. Today* 57 (2004) 39–44.
- [3] M. Carmo, D.L. Fritz, J. Mergel, D. Stolten, A comprehensive review on PEM water electrolysis, *Int. J. Hydrog. Energy* 38 (2013) 4901–4934.
- [4] Y. Guo, T. Park, J.W. Yi, J. Henzie, J. Kim, Z. Wang, B. Jiang, Y. Bando, Y. Sugahara, J. Tang, Y. Yamauchi, Nanoarchitectonics for transition-metal-sulfide-based electrocatalysts for water splitting, *Adv. Mater.* 31 (2019), 1807134.
- [5] Y. Lee, J. Suntivich, K.J. May, E.E. Perry, Y. Shao-Horn, Synthesis and activities of rutile  $IrO_2$  and  $RuO_2$  nanoparticles for oxygen evolution in acid and alkaline solutions, *J. Phys. Chem. Lett.* 3 (2012) 399–404.
- [6] B. Patil, B. Satilmis, M.A. Khalily, T. Uyar, Atomic layer deposition of  $NiOOH/Ni(OH)_2$  on PIM-1-based N-doped carbon nanofibers for electrochemical water splitting in alkaline medium, *ChemSusChem* 12 (2019) 1469–1477.
- [7] L. Ma, Z. Wei, C. Zhao, X. Meng, H. Zhang, M. Song, Y. Wang, B. Li, X. Huang, C. Xu, M. Feng, P. He, D. Jia, Y. Zhou, X. Duan, Hierarchical superhydrophilic/superaerophobic 3D porous trimetallic (Fe, Co, Ni) spinel/carbon/nickel foam for boosting oxygen evolution reaction, *Appl. Catal. B* 332 (2023), 122717.
- [8] M. Karupuraranjith, Y. Chen, B. Wang, J. Ramkumar, D. Yang, K. Srinivas, W. Wang, W. Zhang, R. Manigandan, Hierarchical ultrathin layered  $MoS_2@NiFe_2O_4$  nanohybrids as a bifunctional catalyst for highly efficient oxygen evolution and organic pollutant degradation, *J. Colloid Interface Sci.* 592 (2021) 385–396.
- [9] K. Srinivas, Y. Chen, B. Wang, B. Yu, X. Wang, Y. Hu, Y. Lu, W. Li, W. Zhang, D. Yang, Metal-organic framework-derived  $NiS/Fe_3O_4$  heterostructure-decorated carbon nanotubes as highly efficient and durable electrocatalysts for oxygen evolution reaction, *ACS Appl. Mater. Interfaces* 12 (2020) 31552–31563.
- [10] B. Wang, Y. Chen, X. Wang, J. Ramkumar, X. Zhang, B. Yu, D. Yang, M. Karupuraranjith, W. Zhang, rGO wrapped trimetallic sulfide nanowires as an efficient bifunctional catalyst for electrocatalytic oxygen evolution and photocatalytic organic degradation, *J. Mater. Chem. A* 8 (2020) 13558–13571.
- [11] B. Wang, X. Wang, Z. Wang, K. Srinivas, X. Zhang, B. Yu, D. Yang, W. Zhang, T. Lau, Y. Chen, Electronic modulation of NiS-PBA/CNT with boosted water oxidation performance realized by a rapid microwave-assisted in-situ partial sulfidation, *Chem. Eng. J.* 420 (2021), 130481.
- [12] B. Wang, Y. Hu, B. Yu, X. Zhang, D. Yang, Y. Chen, Heterogeneous  $CoFe-Co_8FeS_8$  nanoparticles embedded in CNT networks as highly efficient and stable electrocatalysts for oxygen evolution reaction, *J. Power Sources* 433 (2019), 126688.
- [13] B. Wang, Y. Chen, X. Wang, X. Zhang, Y. Hu, B. Yu, D. Yang, W. Zhang, A microwave-assisted bubble bursting strategy to grow  $Co_8FeS_8/CoS$  heterostructure on rearranged carbon nanotubes as efficient electrocatalyst for oxygen evolution reaction, *J. Power Sources* 449 (2020), 227561.
- [14] K. Srinivas, Y. Chen, X. Wang, B. Wang, M. Karupuraranjith, W. Wang, Z. Su, W. Zhang, D. Yang, Constructing  $Ni/NiS$  heteronanoparticle-embedded metal-organic framework-derived nanosheets for enhanced water-splitting catalysis, *ACS Sustain. Chem. Eng.* 9 (2021) 1920–1931.
- [15] X. Chen, X. Wang, X. Zhang, K. Srinivas, D. Liu, X. Zhao, H. Yu, B. Wang, W. Zhang, Y. Chen, Vertical  $Fe(OH)_3/Ni_9S_8$  nanoarrays electrodeposited on stainless steel as

binder-free electrocatalyst for highly efficient and stable oxygen evolution reaction, *J. Mater. Sci.* 56 (2021) 19144–19154.

[16] P. Luo, H. Zhang, L. Liu, Y. Zhang, J. Deng, C. Xu, N. Hu, Y. Wang, Targeted Synthesis of unique nickel sulfide (NiS, NiS<sub>2</sub>) microarchitectures and the applications for the enhanced water splitting system, *ACS Appl. Mater. Interfaces* 9 (2017) 2500–2508.

[17] J.O. Bockris, T. Otagawa, The electrocatalysis of oxygen evolution on perovskites, *J. Electrochem. Soc.* 131 (1984) 290–302.

[18] Z. Li, M. Xiao, Y. Zhou, D. Zhang, H. Wang, X. Liu, D. Wang, W. Wang, Pyrite FeS<sub>2</sub>/C nanoparticles as an efficient bi-functional catalyst for overall water splitting, *Dalton Trans.* 47 (2018) 14917–14923.

[19] S. Klaus, M.W. Louie, L. Trotocaud, A.T. Bell, Role of catalyst preparation on the electrocatalytic activity of Ni<sub>1-x</sub>Fe<sub>x</sub>OOH for the oxygen evolution reaction, *J. Phys. Chem. C* 119 (2015) 18303–18316.

[20] Y. Xie, H. Yu, L. Deng, R.S. Amin, D. Yu, A.E. Fetohi, M.Y. Maximov, L. Li, K.M. El-Khatib, S. Peng, Anchoring stable FeS<sub>2</sub> nanoparticles on MXene nanosheets via interface engineering for efficient water splitting, *Inorg. Chem. Front.* 9 (2022) 662–669.

[21] G. Wang, C. Jin, G. Zhang, L. Qian, X. Chen, J. Tan, W. Wang, J. Yin, X. Liu, H. Zhou, Surface self-reconstructed amorphous/crystalline hybrid iron disulfide for high-efficiency water oxidation electrocatalysis, *Dalton Trans.* 50 (2021) 6333–6342.

[22] G. Chen, Z. Hu, Y. Zhu, B. Gu, Y. Zhong, H. Lin, C. Chen, W. Zhou, Z. Shao, A universal strategy to design superior water-splitting electrocatalysts based on fast in situ reconstruction of amorphous nanofilm precursors, *Adv. Mater.* 30 (2018) 1804333.

[23] P. Chen, T. Zhou, S. Wang, N. Zhang, Y. Tong, H. Ju, W. Chu, C. Wu, Y. Xie, Dynamic migration of surface fluorine anions on cobalt-based materials to achieve enhanced oxygen evolution catalysis, *Angew. Chem. Int. Ed.* 57 (2018) 15471–15475.

[24] L. Wang, Q. Zhou, Z. Pu, Q. Zhang, X. Mu, H. Jing, S. Liu, C. Chen, S. Mu, Surface reconstruction engineering of cobalt phosphides by Ru induction to form hollow Ru-Ru<sub>x</sub>-Co<sub>x</sub>P pre-electrocatalysts with accelerated oxygen evolution reaction, *Nano Energy* 53 (2018) 270–276.

[25] Z. Kou, Y. Yu, X. Liu, X. Gao, L. Zheng, H. Zou, Y. Pang, Z. Wang, Z. Pan, J. He, S. J. Pennycook, J. Wang, Potential-dependent phase transition and Mo-enriched surface reconstruction of  $\gamma$ -CoOOH in a heterostructured Co-Mo<sub>2</sub>C precatalyst enable water oxidation, *ACS Catal.* 10 (2020) 4411–4419.

[26] X. Zou, Y. Wu, Y. Liu, D. Liu, W. Li, L. Gu, H. Liu, P. Wang, L. Sun, Y. Zhang, In situ generation of bifunctional, efficient Fe-based catalysts from mackinawite iron sulfide for water splitting, *Chem* 4 (2018) 1139–1152.

[27] T.X. Nguyen, Y.H. Su, C.C. Lin, J.M. Ting, Self-reconstruction of sulfate-containing high entropy sulfide for exceptionally high-performance oxygen evolution reaction electrocatalyst, *Adv. Funct. Mater.* 31 (2021), 2106229.

[28] K. Kawashima, R.A. Márquez, Y.J. Son, C. Guo, R.R. Vaidyula, L.A. Smith, C. E. Chukwunekwe, C.B. Mullins, Accurate potentials of Hg/HgO electrodes: practical parameters for reporting alkaline water electrolysis overpotentials, *ACS Catal.* 13 (2023) 1893–1898.

[29] L. Yu, Z. Ren, Systematic study of the influence of iR compensation on water electrolysis, *Mater. Today Phys.* 14 (2020), 100253.

[30] E.J. Kim, B. Batchelor, Synthesis and characterization of pyrite (FeS<sub>2</sub>) using microwave irradiation, *Mater. Res. Bull.* 44 (2009) 1553–1558.

[31] J. Yu, G. Cheng, W. Luo, Ternary nickel-iron sulfide microflowers as a robust electrocatalyst for bifunctional water splitting, *J. Mater. Chem. A* 5 (2017) 15838–15844.

[32] G. Zhang, Y. Feng, W. Lu, D. He, C. Wang, Y. Li, X. Wang, F. Cao, Enhanced catalysis of electrochemical overall water splitting in alkaline media by Fe doping in Ni<sub>3</sub>S<sub>2</sub> nanosheet arrays, *ACS Catal.* 8 (2018) 5431–5441.

[33] Z. Jing, Q. Zhao, D. Zheng, L. Sun, J. Geng, Q. Zhou, J. Lin, Nickel-doped pyrrhotite iron sulfide nanosheets as highly efficient electrocatalyst for water splitting, *J. Mater. Chem. A* 8 (2020) 20323–20330.

[34] N. Yang, C. Tang, K. Wang, G. Du, A.M. Asiri, X. Sun, Iron-doped nickel disulfide nanoarray: a highly efficient and stable electrocatalyst for water splitting, *Nano Res.* 9 (2016) 3346–3354.

[35] Y. Liu, S. Yin, P.K. Shen, Asymmetric 3d electronic structure for enhanced oxygen evolution catalysis, *ACS Appl. Mater. Interfaces* 10 (2018) 23131–23139.

[36] Y. Liu, X. Xie, G. Zhu, Y. Mao, Y. Yu, S. Ju, X. Shen, H. Pang, Small sized Fe-Co sulfide nanoclusters anchored on carbon for oxygen evolution, *J. Mater. Chem. A* 7 (2019) 15851–15861.

[37] Z. Tan, L. Sharma, R. Kakkar, T. Meng, Y. Jiang, M. Cao, Arousing the reactive Fe sites in pyrite (FeS<sub>2</sub>) via integration of electronic structure reconfiguration and in situ electrochemical topotactic transformation for highly efficient oxygen evolution reaction, *Inorg. Chem.* 58 (2019) 7615–7627.

[38] M.J. Wang, X. Zheng, L. Song, X. Feng, Q. Liao, J. Li, L. Li, Z. Wei, Fe<sub>3</sub>O<sub>4</sub>/FeS<sub>2</sub> heterostructures enable efficient oxygen evolution reaction, *J. Mater. Chem. A* 8 (2020) 14145–14151.

[39] X. Ding, W. Li, H. Kuang, M. Qu, M. Cui, C. Zhao, D.C. Qi, F.E. Oropeza, K. Zhang, An Fe stabilized metallic phase of NiS<sub>2</sub> for the highly efficient oxygen evolution reaction, *Nanoscale* 11 (2019) 23217–23225.

[40] X. Luan, H. Du, Y. Kong, F. Qu, L. Lu, A novel FeS-NiS hybrid nanoarray: an efficient and durable electrocatalyst for alkaline water oxidation, *Chem. Commun.* 55 (2019) 7335–7338.

[41] S. Chen, Z. Kang, X. Zhang, J. Xie, H. Wang, W. Shao, X. Zheng, W. Yan, B. Pan, Y. Xie, Highly active Fe sites in ultrathin pyrrhotite Fe<sub>x</sub>S<sub>8</sub> nanosheets realizing efficient electrocatalytic oxygen evolution, *ACS Cent. Sci.* 3 (2017) 1221–1227.

[42] K. Pan, Y. Zhai, J. Zhang, K. Yu, FeS<sub>2</sub>/C nanowires as an effective catalyst for oxygen evolution reaction by electrolytic water splitting, *Materials* 12 (2019) 3364.

[43] B. Jansi Rani, P. Aiswarya Kanjana, G. Ravi, R. Yuvakkumar, B. Saravanakumar, Superior electrochemical water oxidation of novel NiS@FeS<sub>2</sub> nanocomposites, *Mater. Sci. Semicond. Process.* 101 (2019) 174–182.

[44] J. Jiang, S. Lu, H. Gao, X. Zhang, H. Yu, Ternary FeNiS<sub>2</sub> ultrathin nanosheets as an electrocatalyst for both oxygen evolution and reduction reactions, *Nano Energy* 27 (2016) 526–534.

[45] J. Chen, F. Zheng, S. Zhang, A. Fisher, Y. Zhou, Z. Wang, Y. Li, B. Xu, J. Li, S. Sun, Interfacial interaction between FeOOH and Ni-Fe LDH to modulate the local electronic structure for enhanced OER electrocatalysis, *ACS Catal.* 8 (2018) 11342–11351.

[46] P. Zhang, L. Li, D. Nordlund, H. Chen, L. Fan, B. Zhang, X. Sheng, Q. Daniel, L. Sun, Dendritic core-shell nickel-iron-copper metal/metal oxide electrode for efficient electrocatalytic water oxidation, *Nat. Commun.* 9 (2018) 381.

[47] X. Yan, W. Zhang, H. Xu, B. Liu, M. Hu, J. Liu, Z. Gu, Surface metal-EDTA coordination layer activates Ni<sub>x</sub>Fe<sub>3-x</sub>O<sub>4</sub> spinel as an outstanding electrocatalyst for oxygen evolution reaction, *J. Colloid Interface Sci.* 632 (2023) 44–53.

[48] L. He, Z. Li, M. Gao, G. Sheng, Phosphorus-accumulating organism assisted phosphorization of Ni-Fe nanocomposites for efficient oxygen evolution reaction, *ACS Sustain. Chem. Eng.* 8 (2020) 11456–11464.

[49] F. Yu, H. Zhou, Y. Huang, J. Sun, F. Qin, J. Bao, W.A. Goddard, S. Chen, Z. Ren, High-performance bifunctional porous non-noble metal phosphide catalyst for overall water splitting, *Nat. Commun.* 9 (2018) 2551.

[50] H. Zhou, F. Yu, Q. Zhu, J. Sun, F. Qin, L. Yu, J. Bao, Y. Yu, S. Chen, Z. Ren, Water splitting by electrolysis at high current densities under 1.6 volts, *Energy Environ. Sci.* 11 (2018) 2858–2864.

[51] Z. Lin, P. Bu, Y. Xiao, Q. Gao, P. Diao,  $\beta$ -and  $\gamma$ -NiFeOOH electrocatalysts for an efficient oxygen evolution reaction: an electrochemical activation energy aspect, *J. Mater. Chem. A* 10 (2022) 20847–20855.

[52] O. Schmidt, A. Gambhir, I. Staffell, A. Hawkes, J. Nelson, S. Few, Future cost and performance of water electrolysis: an expert elicitation study, *Int. J. Hydron. Energy* 42 (2017) 30470–30492.

[53] M. Carmo, D.L. Fritz, J. Mergel, D. Stolten, A comprehensive review on PEM water electrolysis, *Int. J. Hydron. Energy* 38 (2013) 4901–4934.

[54] H. Radinger, P. Connor, S. Tengeler, R.W. Stark, W. Jaegermann, B. Kaiser, Importance of nickel oxide lattice defects for efficient oxygen evolution reaction, *Chem. Mater.* 33 (2021) 8259–8266.

[55] M. Fingerle, S. Tengeler, W. Calvet, W. Jaegermann, T. Mayer, Sputtered nickel oxide thin films on n-Si(100)/SiO<sub>2</sub> surfaces for photo-electrochemical oxygen evolution reaction (OER): impact of deposition temperature on OER performance and on composition before and after OER, *J. Electrochem. Soc.* 167 (2020), 136514.

[56] D.S. Hall, C. Bock, B.R. MacDougall, The electrochemistry of metallic nickel: oxides, hydroxides, hydrides and alkaline hydrogen evolution, *J. Electrochem. Soc.* 160 (2013) F235–F243.

[57] N. Suen, S. Hung, Q. Quan, N. Zhang, Y. Xu, H.M. Chen, Electrocatalysis for the oxygen evolution reaction: recent development and future perspectives, *Chem. Soc. Rev.* 46 (2017) 337–365.

[58] X. Luo, L. Zhang, M. Guo, Z. Liu, D. Wu, D. Zhen, Y. Liu, Engineering the structural defects of spinel oxide nanoneedles by doping of V for a highly efficient oxygen evolution reaction, *ACS Appl. Mater. Interfaces* 14 (2022) 50055–50067.

[59] X. Chen, Y. Zeng, Z. Chen, S. Wang, C. Xin, L. Wang, C. Shi, L. Lu, C. Zhang, Synthesis and electrochemical property of FeOOH/graphene oxide composites, *Front. Chem.* 8 (2020) 328.

[60] D.L. De Faria, S. Venâncio Silva, M.T. De Oliveira, Raman microspectroscopy of some iron oxides and oxyhydroxides, *J. Raman Spectrosc.* 28 (1997) 873–878.

[61] J.G. McAlpin, Y. Surendranath, M. Dincă, T.A. Stich, S.A. Stoian, W.H. Casey, D. G. Nocera, R.D. Britt, EPR evidence for Co(IV) species produced during water oxidation at neutral pH, *J. Am. Chem. Soc.* 132 (2010) 6882–6883.

[62] X. Wu, X. Song, H. Tan, Y. Kang, Z. Zhao, S. Jin, X. Chang, Deciphering the structure evolution and active origin for electrochemical oxygen evolution over Ni<sub>3</sub>S<sub>2</sub>, *Mater. Today Energy* 26 (2022), 101008.

[63] C. Kung, H. Chen, C. Lin, K. Huang, R. Vittal, K. Ho, CoS acicular nanorod arrays for the counter electrode of an efficient dye-sensitized solar cell, *ACS Nano* 6 (2012) 7016–7025.

[64] H. Liao, T. Luo, P. Tan, K. Chen, L. Lu, Y. Liu, M. Liu, J. Pan, Unveiling role of sulfate ion in nickel-iron (oxy) hydroxide with enhanced oxygen-evolving performance, *Adv. Funct. Mater.* 31 (2021), 2102772.

[65] L. Zhuang, L. Ge, Y. Yang, M. Li, Y. Jia, X. Yao, Z. Zhu, Ultrathin iron-cobalt oxide nanosheets with abundant oxygen vacancies for the oxygen evolution reaction, *Adv. Mater.* 29 (2017), 1606793.

[66] L. Xu, Q. Jiang, Z. Xiao, X. Li, J. Huo, S. Wang, L. Dai, Plasma-engraved Co<sub>3</sub>O<sub>4</sub> nanosheets with oxygen vacancies and high surface area for the oxygen evolution reaction, *Angew. Chem. Int. Ed.* 55 (2016) 5277–5281.

[67] Q. He, H. Xie, Z.U. Rehman, C. Wang, P. Wan, H. Jiang, W. Chu, L. Song, Highly defective Fe-based oxyhydroxides from electrochemical reconstruction for efficient oxygen evolution catalysis, *ACS Energy Lett.* 3 (2018) 861–868.

[68] G. Park, Y.I. Kim, Y.H. Kim, M. Park, K.Y. Jang, H. Song, K.M. Nam, Preparation and phase transition of FeOOH nanorods: strain effects on catalytic water oxidation, *Nanoscale* 9 (2017) 4751–4758.